An Island Scanning Path-Patten Optimization for Metal Additive Manufacturing Based on Inherent Strain Method

Shuzhi Xu[1], Jiaqi Huang[2], Jikai Liu[2] and Yongsheng Ma[1]

[1]University of Alberta, yongsheng.ma@ualberta.ca
[2]Shandong University, jikai_liu@sdu.edu.cn

Corresponding authors: Yongsheng Ma, yongsheng.ma@ualberta.ca
Jikai Liu, jikai_liu@sdu.edu.cn

Abstract. Since it is quite easy to set or adjust such island scanning path of the laser for the metal AM machine, a systemic metal AM oriented island-type scanning pattern optimization method is therefore proposed in this paper. This method consists of a non-constraint optimization model and an inherent strain method model, which could effectively reduce the maximum distortion induced by the metal manufacturing process. The proposed method is used to optimize the island scanning path for a printed fan blade part, and numerical experimental results show that the part printed by optimized path can achieve nearly 50% reduction in part deflection compared with the part printed by default path.

Keywords: Metal additive manufacturing, scanning path optimization, inherent strain method.
DOI: https://doi.org/10.14733/cadaps.2022.812-824

1 INTRODUCTION

Additive manufacturing (AM) is the fastest-growing segment of manufacturing technologies in past decades. The end-use products fabricated by the AM are increasingly being used in many industries like aerospace, automotive, machinery, and biomedical [11,16,17,18,19,26].

This concept has been developed for different materials like plastic and metal, with an adaptation of the process **Error! Reference source not found.**. Among processes, powder bed fusion (PBF) has the capability to build metal objects with complex geometries, and thus has captured the interest of the researchers and industry experts **Error! Reference source not found.**. During this manufacturing process: a source of thermal energy (laser) moves along a planned trajectory, and meanwhile selectively fuses the regularly distributed powder. Then the material solidifies from cooling, and a new layer of powder is spread across the previous layer. Further layers are fused and added until the entire model is created.

However, the residual stress will be accumulated during the manufacturing process of PBF due to inconsistent level of heating. Consequently, severe issues such as cracks and significant distortion (Figure 1) may appear which affect the manufacturing process and reduce the part quality [5-6]. There are many researches proposed to resolve above mentioned challenges. **Error! Reference source not found.** proposed a topology optimization scheme to minimize the mean compliance and the part distortion, and a thermo-elastic element-birth model is adopted in this method to better describe the AM process. Besides, a layer-by-layer thermo-elastic model was constructed and incorporated with the level set topology optimization method in to constraint the structural thermal stress **Error! Reference source not found.**. Reasonable results have been achieved in both approaches. However, the above methods, when extended to practical 3D problems, will involve computationally intensive transient thermo-mechanical analysis with very fine mesh corresponding to the laser spot size, which makes the iterative finite element analysis computationally unaffordable. Hence, the inherent strain-based method (ISM), as a simplified AM process simulation solver is highly concentrated, has been adopted by commercial software tools and academic researches to be a computationally reasonable simulation tool for 3D PBF process **Error! Reference source not found.**. A variety of studies utilized the ISM to optimize the structures in order to reduce the residual stress or distortion **Error! Reference source not found.**. In the ISM, the printed part is sliced into layers that are sequentially activated with the corresponding inherent strain in macroscale, then the static finite analysis will be conducted layer by layer. Differently oriented inherent strains could be activated by different scanning paths in each layer, and thus affects the printing quality of part. The influence on thermal residual stress or distortion of different scanning orientations have been widely explored in many researches **Error! Reference source not found.**. Recently, a continuous scanning path optimization method to against the residual stress/distortion is proposed in **Error! Reference source not found.**. However, the optimized paths obtained by the authors are complex, and hard to be adopted in real application.

In this work, a systemic metal AM oriented island-type scanning pattern optimization method, which could reduce the maximum distortion during the manufacturing process, is proposed by us. First, to avoid the mesh regeneration in the optimization iterations, a voxel-based methodology is employed to generate efficient Cartesian mesh of the printed part for finite element analysis. Instead of using full-scale thermal-elastic simulation, for the purpose of saving computational cost, a layer-by-layer ISM is adopted to efficiently describe the complex physical behavior during the AM process. Then, a non-constraint optimization problem is formulated to find the optimal island scanning path in each print layer. The stability-based aggregation method is adopted to explicitly describe the maximum distortion. Then the sensitivity analysis is achieved with the adjoint method as well as validated by the forward finite difference method (FFDM). In the end, a numerical example is provided, which indicates the effectiveness of this method.

In practice, it is quite easy to set or adjust such island scanning path of the laser for the metal AM machine, and the non-constraint optimization model also ensures the robustness of the algorithm. The proposed method therefore could be broadly applied in metal AM industry.

2 INHERENT STRAIN METHOD

During the heating and cooling cycle of the metal AM processes, the total strain $\boldsymbol{\epsilon}^{\mathrm{tatal}}$ could be split into elastic strains $\boldsymbol{\epsilon}^{\mathrm{elastic}}$, thermal strains $\boldsymbol{\epsilon}^{\mathrm{thermal}}$, plastic strains $\boldsymbol{\epsilon}^{\mathrm{plastic}}$, phase transformation strains $\boldsymbol{\epsilon}^{\mathrm{phase}}$ and creep strains $\boldsymbol{\epsilon}^{\mathrm{creep}}$, and expressed as:

$$\boldsymbol{\epsilon}^{\mathbf{tatal}} = \boldsymbol{\epsilon}^{\mathbf{elastic}} + \boldsymbol{\epsilon}^{\mathbf{thermal}} + \boldsymbol{\epsilon}^{\mathbf{plastic}} + \boldsymbol{\epsilon}^{\mathbf{phase}} + \boldsymbol{\epsilon}^{\mathbf{creep}} \tag{2.1}$$

Recalling the balance of momentum equation for a quasi-static analysis, we arrive:

$$\boldsymbol{\nabla\sigma} + \mathbf{b} = 0 \tag{2.2}$$

where b is the body force vector. When defining the inherent strain as: $\boldsymbol{\epsilon}^{\mathrm{ihs}} = \boldsymbol{\epsilon}^{\mathrm{thermal}} + \boldsymbol{\epsilon}^{\mathrm{plastic}} + \boldsymbol{\epsilon}^{\mathrm{phase}} + \boldsymbol{\epsilon}^{\mathrm{creep}}$, the constitutive equation could be written as:

$$\boldsymbol{\sigma} = \mathbf{D}\left(\boldsymbol{\epsilon}^{\mathbf{tatal}} - \boldsymbol{\epsilon}^{\mathbf{ihs}}\right) \tag{2.3}$$

To reduce the computational cost, the components of original eigen inherent strain tensor $\boldsymbol{\epsilon}^{\mathrm{ihs}}$ could be directly obtained by experimental calibration or high-fidelity simulation method **Error! Reference source not found.**. By rotating the direction of original inherent strain $\boldsymbol{\epsilon}^{\mathrm{ihs0}}$, the elemental inherent strain $\boldsymbol{\epsilon}^{*}{}_{e}$ in each scanned island (Figure 1**Error! Reference source not found.**) could be expressed as:

$$\boldsymbol{\epsilon}^{*}{}_{e} = \mathbf{R}\boldsymbol{\epsilon}^{\mathrm{ihs0}}\mathbf{R}^{\mathrm{T}} \tag{2.4}$$

where $\mathbf{R}$ is the xy-plane rotation matrix, which could be expressed as a function of the elemental orientation angle ϑ_e:

$$\boldsymbol{R} = \begin{bmatrix} cos(\vartheta_e) & sin(\vartheta_e) & 0 \\ -sin(\vartheta_e) & cos(\vartheta_e) & 0 \\ 0 & 0 & 1 \end{bmatrix} \tag{2.5}$$

Note that there is a mapping relationship between the island-wise orientation angle $\boldsymbol{\theta}$ and element-wise orientation angle $\boldsymbol{\vartheta}$:

$$\boldsymbol{\vartheta} = \mathbf{M}\boldsymbol{\theta} \tag{2.6}$$

where the $\mathbf{M}$ is $0-1$ mapping matrix with $\mathrm{Nel} \times \mathrm{Nd}$ dimensions, Nel is the total number of finite elements in this model, and Nd is the total number of design variables (the number of scanning island).

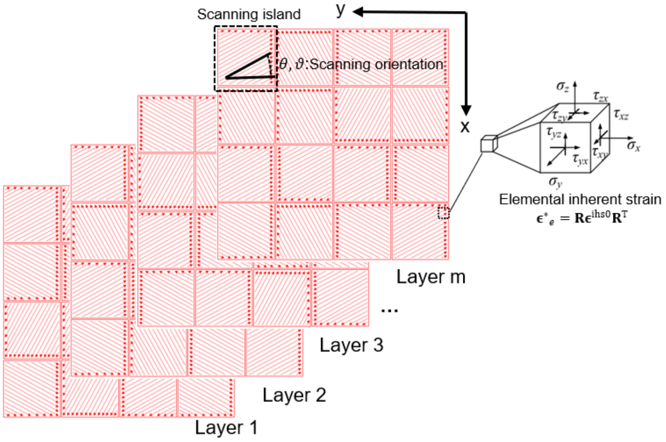

Figure 1: Illustration of rotated inherent strains in different print layers.

3 INHERENT STRAIN METHOD

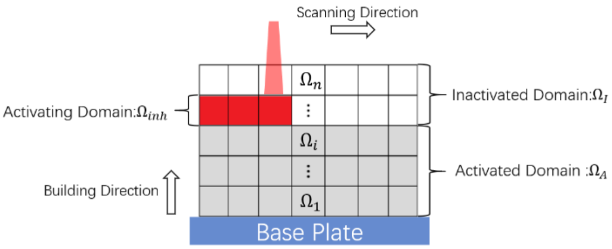

Figure 2: Short, centered caption, terminated with a full stop.

As shown in the Figure 2, the domain Ω is divided into m layers with a fixed thickness along the building direction. Each layer is defined by Ω_i and $1 \leq \mathrm{i} \leq \mathrm{m}$. The domain Ω is composed by three subdomains, where represented by Ω_ihs, Ω_act, and Ω_pass. Ω_ihs is the layer to be printed and to apply the inherent strain, Ω_act is the already printed layers, and Ω_pass is the unprinted layers. It is reasonable to assume the inherent strain $\boldsymbol{\epsilon}^*$ at the domain Ω_ihs contributes to the distortion in the rest part of the substrate. Within above assumptions, the displacements $\mathbf{U}^\mathrm{i}$ of printing stage i are calculated as follows:

$$\mathbf{K}^\mathrm{i}\mathbf{U}^\mathrm{i} = \mathbf{F}^\mathrm{i} \tag{3.1}$$

where

$$\mathbf{F}^\mathrm{i} = \sum_{\mathrm{e}=1}^{\mathrm{Nel}} \left(\vartheta_\mathrm{e}^\mathrm{i} \mathbf{L}_\mathrm{e}^\mathrm{T} \int \mathbf{B}^\mathrm{T} \mathbf{D}_0 \boldsymbol{\epsilon}^*{}_e \, \mathrm{d}\Omega_\mathrm{e} \right) \tag{3.2}$$

and

$$\mathbf{K}^{\mathrm{i}} = \sum_{\mathrm{i}=1}^{\mathrm{m}}\left(\sum_{\mathrm{e}=1}^{\mathrm{Nel}}\left(\delta_{\mathrm{e}}^{\mathrm{i}}\mathbf{L}_{\mathrm{e}}^{\mathrm{T}}\mathbf{K}_0\mathbf{L}_{\mathrm{e}}\right)\right) \tag{3.3}$$

$\vartheta_{\mathrm{e}}^{\mathrm{i}}$ and $\delta_{\mathrm{e}}^{\mathrm{i}}$ are two flag variables to indicate the domain Ω_{ihs} and Ω_{act}, the matrix $\mathbf{L}_{\mathrm{e}}$ gathers the nodal displacements of the eth element ($\mathbf{u}_{\mathrm{e}}$) from the global displacement vector ($\mathbf{U}$) satisfying $\mathbf{u}_{\mathrm{e}} = \mathbf{L}_{\mathrm{e}}\mathbf{U}$, and $\mathbf{K}_0$ is the elemental stiffness matrix which is calculated as follows:

$$\mathbf{K}_{\mathrm{e}} = \int \mathbf{B}^{\mathrm{T}}\mathbf{D}_0\,\mathbf{B}\,\mathrm{d}\Omega_{\mathrm{e}} \tag{3.4}$$

where $\mathbf{B}$ is the strain-displacement matrix, and $\mathbf{D}_0$ is the constitutive matrix for the solid material. The part-scale displacement for a specific printing stage i is determined as a sum of the displacements all layers printed so far:

$$\mathbf{U} = \sum_{\mathrm{i}=1}^{\mathrm{m}}\mathbf{U}^{\mathrm{i}} \tag{3.5}$$

This layer-by-layer manner could be illustrated in Figure 3.

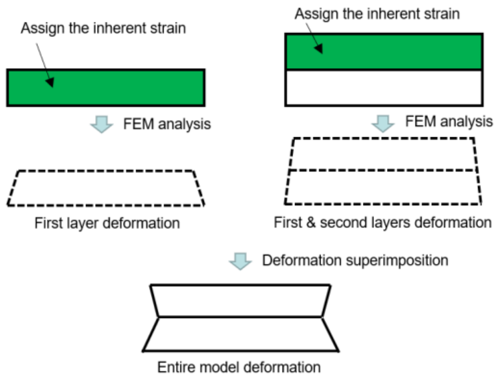

Figure 3: Two-layer example for illustration of the layer-by-layer method of assigning the inherent strain and deformation calculation.

To visualize the additive manufacturing process, the part-scale deformation simulations of the cantilever beam (Figure 4) under $180°$ scanning strategies are provided in Figure 5. The building platform was not considered in the model since it was represented by a fully constrained bottom region. The layer lumping strategy is adopted in this work, which enables to use a relatively coarse FE mesh. It is only meshed with 3750 structured hexahedral elements. The material adopted in this work is Ti6Al4V, which has Young's modulus of 110 GPa, Poisson's ratio of 0.3. In this work, the original inherent strain $\boldsymbol{\epsilon}^{\mathrm{ihs0}}$ is set as $[-0.002,\ -0.001, 0]$.

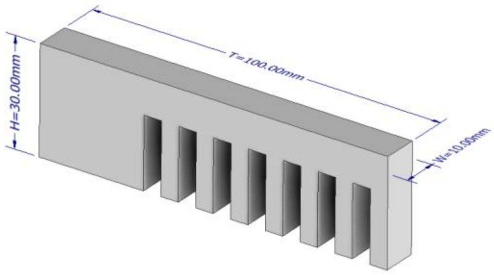

Figure 4: The dimension of cantilever beam.

Higher distortion is observed at the out part of support beam interface, which meets the actual results observed in real experiment.

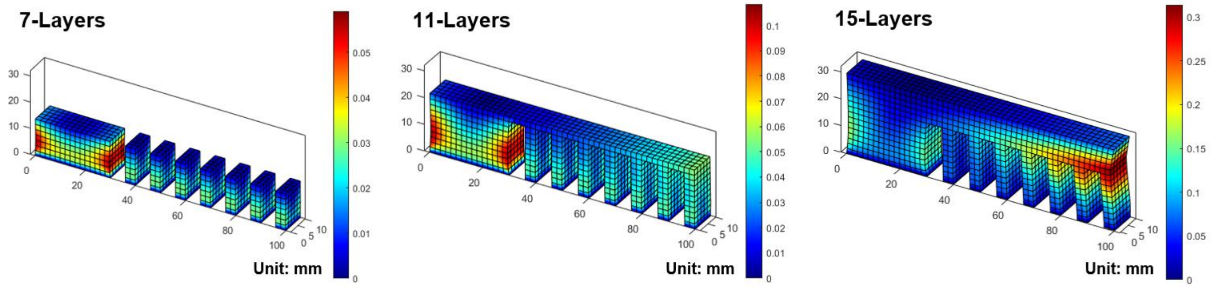

Figure 5: The part-scale deformation results of the cantilever beam.

4 NON-CONSTRAINT OPTIMIZATION PROBLEM FORMULATION

4.1.1 Non-constraint optimization problem formulation

For the optimization problem, the objective function is formulated to minimize the maximum structural distortion under the inherent strain load. The mathematical formulation of this optimization problem can be expressed as follows:

$$\begin{aligned} &\text{find: } \boldsymbol{\theta} = \{\theta_k\} \ (k = 1,2,3,\dots,Nd) \\ &\text{minimize: } J = U_{max}(\boldsymbol{\theta}) \\ &\text{subject to: } \begin{cases} \mathbf{K}^i\mathbf{u}^i = \mathbf{F}^i \ (i = 1,2,\dots,m) \\ 0° \le \forall\theta \le 180° \end{cases} \end{aligned} \tag{4.1}$$

U_{max} indicates the maximum displacement, which can be restated in terms of a single differentiable global quantity through the aggregation method. The P-norm aggregation function is adopted in this work, and the maximum displacement could be approximately expressed as:

$$U_{max} \approx U_{PN} = \left(\sum_{n=1}^{Nod}(U_n)^P\right)^{\frac{1}{P}} \tag{4.2}$$

U_{PN} is the global P-norm measure, U_n is the displacement in the nth node, P is the aggregation parameter, and Nod is the total number of nodes. Ideally, the P-norm measure approaches the maximum value when $P \to \infty$. However, a large P value easily tends to make optimization problem ill-conditioned. Relatively small P value is preferred in practice given the convergence stability which however, leads to the gap between the exact and the approximated maximum value. Therefore, to better approximate the maximum displacement without overly increasing the P value, the global P-norm stress measure is iteratively corrected through:

$$\overline{U}_{PN} = c \cdot U_{PN} \tag{4.3}$$

where c is the correction parameter at the Ith iteration $(I > 1)$ that reflects the ratio of the maximum von Mises stress to the P-norm stress from the current iteration. Note that, the change of c would be jumping if only taking the history-independent maximum displacement ratio to make the correction, causing oscillations and instabilities of the convergence. To address this issue, a parameter α^I ($\alpha^I \in (0,1]$) is added to restrict the variation between c^I and c^{I-1}, as demonstrated below:

$$c^I = \alpha^I \cdot \frac{\max(\forall U_n)}{U_{PN}^I} + (1 - \alpha^I) \cdot c^{I-1} \tag{4.4}$$

In this work, $\alpha^I = 0.5$ is adopted for all iterations and $c^0 = 1$ is used. Finally, the aggregated maximum nodal displacement could be expressed as:

$$\overline{U}_{PN} = c \cdot \left(\sum_{n=1}^{Nod}(U_n)^P\right)^{\frac{1}{P}} \tag{4.5}$$

4.1.2 Sensitivity analysis

The Method of Moving Asymptotes (MMA) will be adopted to solve the optimization problem, which requires first order sensitivity information of the objective function. The gradients of $\overline{\mathrm{U}}_{\mathrm{PN}}$ are derived following the chain rule, as:

$$\frac{\partial \overline{\mathrm{U}}_{\mathrm{PN}}}{\partial \theta_{\mathrm{k}}} = \mathrm{c} \cdot \sum_{\mathrm{n}=1}^{\mathrm{Nod}} \left(\frac{\partial \mathrm{U}_{\mathrm{PN}}}{\partial \mathrm{U}_{\mathrm{n}}} \frac{\partial \mathrm{U}_{\mathrm{n}}}{\partial \theta_{\mathrm{k}}} \right) \tag{4.6}$$

By differentiating U_{PN} with respect to the nodal displacement, we could arrive:

$$\frac{\partial \mathrm{U}_{\mathrm{PN}}}{\partial \mathrm{U}_{\mathrm{n}}} = \frac{1}{\mathrm{P}} \cdot \left[\sum_{\mathrm{n}=1}^{\mathrm{Nod}} (\mathrm{U}_{\mathrm{n}})^{\mathrm{P}} \right]^{\left(\frac{1}{\mathrm{P}}-1\right)} \cdot \mathrm{P} \cdot (\mathrm{U}_{\mathrm{n}})^{(\mathrm{P}-1)} \tag{4.7}$$

For the term $\frac{\partial \mathrm{U}_{\mathrm{n}}}{\partial \theta_{\mathrm{k}}}$, we could arrive:

$$\frac{\partial \mathrm{U}_{\mathrm{n}}}{\partial \theta_{\mathrm{k}}} = \sum_{\mathrm{i}=1}^{\mathrm{m}} \frac{\partial \mathrm{U}_{\mathrm{n}}^{\mathrm{i}}}{\partial \theta_{\mathrm{k}}} \tag{4.8}$$

The adjoint method will be adopted to address the unknown term $\frac{\partial \mathrm{U}_{\mathrm{n}}^{\mathrm{i}}}{\partial \theta_{\mathrm{k}}}$. Specifically, for the i^{th} layer in additive manufacturing process, we have: $\mathbf{K}^{\mathrm{i}}\mathbf{U}^{\mathrm{i}} = \mathbf{F}^{\mathrm{i}}$. Taking derivatives of both sides of the balance equation yields:

$$\mathbf{K}^{\mathrm{i}} \frac{\partial \mathbf{U}^{\mathrm{i}}}{\partial \theta_{\mathrm{k}}} = \frac{\partial \mathbf{F}^{\mathrm{i}}}{\partial \theta_{\mathrm{k}}} \tag{4.9}$$

Then, we could derive the following formula:

$$\frac{\partial \mathbf{u}_{\mathrm{n}}^{\mathrm{i}}}{\partial \theta_{\mathrm{k}}} = \mathbf{L}_{\mathrm{n}} \left(\mathbf{K}^{\mathrm{i}} \right)^{-1} \frac{\partial \mathbf{F}^{\mathrm{i}}}{\partial \theta_{\mathrm{k}}} \tag{4.10}$$

where $\mathbf{L}_{\mathrm{n}}$ is the global-nodal mapping matrix, and for the term $\frac{\partial \mathbf{F}^{\mathrm{i}}}{\partial \theta_{\mathrm{k}}}$:

$$\frac{\partial \mathbf{F}^{\mathrm{i}}}{\partial \theta_{\mathrm{k}}} = \sum_{\mathrm{e}=1}^{\mathrm{Nel}} \left(\vartheta_{\mathrm{e}}^{\mathrm{i}} \mathbf{L}_{\mathrm{e}}^{\mathrm{T}} \int \mathbf{B}^{\mathrm{T}} \mathbf{D}_0 \frac{\partial \epsilon^*{}_e}{\partial \theta_{\mathrm{k}}} \mathrm{d}\Omega_{\mathrm{e}} \right) \tag{4.11}$$

recalling the relationship between the island-wise orientation angle $\boldsymbol{\theta}$ and element-wise orientation angle $\boldsymbol{\vartheta}$, we could further arrive:

$$\frac{\partial \mathbf{F}^{\mathrm{i}}}{\partial \theta_{\mathrm{k}}} = \mathbf{M} \sum_{\mathrm{e}=1}^{\mathrm{Nel}} \left(\vartheta_{\mathrm{e}}^{\mathrm{i}} \mathbf{L}_{\mathrm{e}}^{\mathrm{T}} \int \mathbf{B}^{\mathrm{T}} \mathbf{D}_0 \frac{\partial \epsilon^*{}_e}{\partial \vartheta_{\mathrm{e}}} \mathrm{d}\Omega_{\mathrm{e}} \right) \tag{4.12}$$

Substituting the preceding relation into (4.12) and introducing the adjoint variable $\boldsymbol{\lambda}^{\mathrm{i}}$ yields:

$$\frac{\partial \overline{\mathrm{U}}_{\mathrm{PN}}}{\partial \theta_{\mathrm{k}}} = \mathrm{c} \cdot \sum_{\mathrm{i}=1}^{\mathrm{m}} \left({\boldsymbol{\lambda}^{\mathrm{i}}}^{\mathrm{T}} \mathbf{M} \sum_{\mathrm{e}=1}^{\mathrm{Nel}} \left(\vartheta_{\mathrm{e}}^{\mathrm{i}} \mathbf{L}_{\mathrm{e}}^{\mathrm{T}} \int \mathbf{B}^{\mathrm{T}} \mathbf{D}_0 \frac{\partial \epsilon^*{}_e}{\partial \vartheta_{\mathrm{e}}} \mathrm{d}\Omega_{\mathrm{e}} \right) \right) \tag{4.13}$$

where the adjoint variable is determined by the solution of the adjoint problem:

$$\mathbf{K}^{\mathrm{i}} \boldsymbol{\lambda}^{\mathrm{i}} = \sum_{\mathrm{n}=1}^{\mathrm{Nod}} \left(\frac{\partial \mathrm{U}_{\mathrm{PN}}}{\partial \mathrm{U}_{\mathrm{n}}} \mathbf{L}_{\mathrm{n}} \right) \tag{4.14}$$

4.1.3 Validation of sensitivity analysis

The analytical sensitivity analysis formulation for the sensitivity analysis given by (4.6) to (4.14) is validated against FFDM. A square domain meshed by $4 \times 4 \times 4$ elements with $\mathrm{L}, \mathrm{W}, \mathrm{H} = 1\mathrm{mm}$. The displacement of all the bottom nodes is fixed and the external strain is applied by a layer-by-layer process as mentioned in section 2. The domain in Figure 6 is divided into 4 layers, with a layer thickness of 0.25 mm. The FFDM results are presented with a perturbation size of 1e-4. The validation of sensitivity analysis is conducted at 3 specified elements (red points), whose locations are shown in Figure 6.

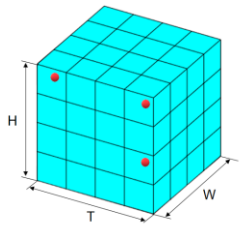

Figure 6: The locations of 3 specific elements.

The sensitivity of the aggregated residual stress measures $\frac{\partial \bar{\mathrm{U}}_{\mathrm{PN}}}{\partial \theta_{\mathrm{k}}}$ with respect to 3 elements are shown in Figure 7. In each plot, the analytical sensitivity given by solid lines and finite difference validation points indicated by filled dots, and perfect agreements could be observed from them.

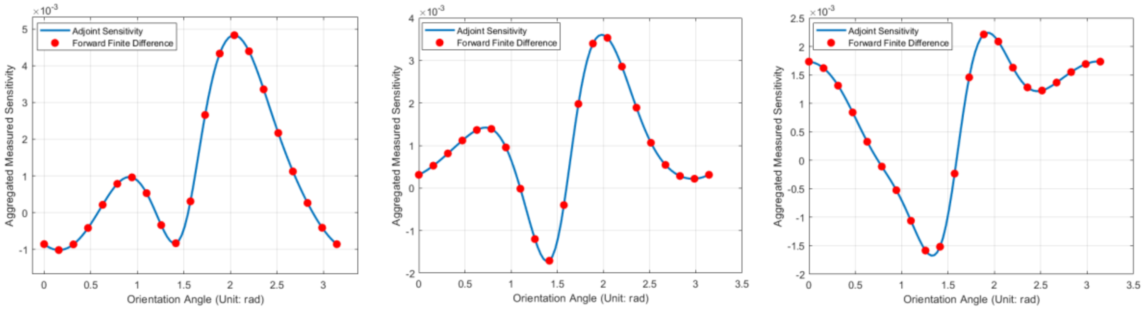

Figure 7: Verification of the analytical sensitivity through a comparison with the finite difference sensitivity for the three specific elements.

5 NUMERICAL IMPLEMENTATION

The flowchart of the proposed optimization approach is illustrated in Figure 8. In the first stage, the STL model of the printed part will be constructed by commercial software. In the next stage, a voxel-based methodology is employed to generate efficient structured hexahedral elements. Then, the initialization of design and optimization parameters will be conducted. After initialization, the ISM based layer-by-layer finite element model is constructed to simulate the structural physical behavior during the PBF process. The sensitivity analysis introduced in section 4.1.2 will be performed in the next stage. Subsequently, MMA optimizer will be adopted to update the design variables. The optimization will terminate when the objective value cannot be further improved. Namely, the difference of the objective values within three successive iterations is less than 0.001, and the constraints are satisfied or the maximum iterative number (400) is exceeded.

6 NUMERICAL CASE STUDY

The numerical example is a fan blade with complex geometry used in mining machinery industry (Figure 9). For the outer section of the model, the length and width are 100 mm. The height of the entire component is 60 mm, indicating around 2160 thin layers in the large part. The whole model has been meshed by 6e5 first order Hexahedron elements of size $1 \times 1 \times 1\,\mathrm{mm}$, and its voxelized mesh model is shown in Figure 10. The material properties are the same with the case shown in section 3.

In the solution process, the default build direction is down-top; and the inherent strain is applied to the blade part with 60 equivalent layers employed, each having 36 physical layers merged together. In each print layer, there are 10×10 scanning islands. The optimization process using 10 Intel Xeon E5-1660 cores with 64GB RAM in a desktop computer. Because of the large number of elements, it took around 25 mins in each iteration.

Firstly, this part is simulated by all scanning islands with the same scanning orientation $180°$. Figure 11 (a) presents the simulation result containing the part-scale distortion distribution for the as-fabricated part. Larger distortions are concentrated at the outer edges of some blades, and the maximum distortion is $3.15\,\mathrm{mm}$.

Figure 11 (b) presents the part-scale distortion distribution for the as-fabricated part with optimized scanning path, and scanning paths for different layers are shown in Figure 12. Recalling that in our optimization problem formulation, the objective is to reduce the maximum part-scale distortion. Therefore, more even residual distortion distribution could be observed in the as-fabricated part, although the higher distortions are still distributed at outer edges of blades. Specifically, the part printed by optimized scanning path exhibits apparently smaller deformation (i.e., the maximum distortion is $u_{max} = 1.83$ mm) compared to the part in Figure 11 (a), $u_{max} = 3.15$ mm.

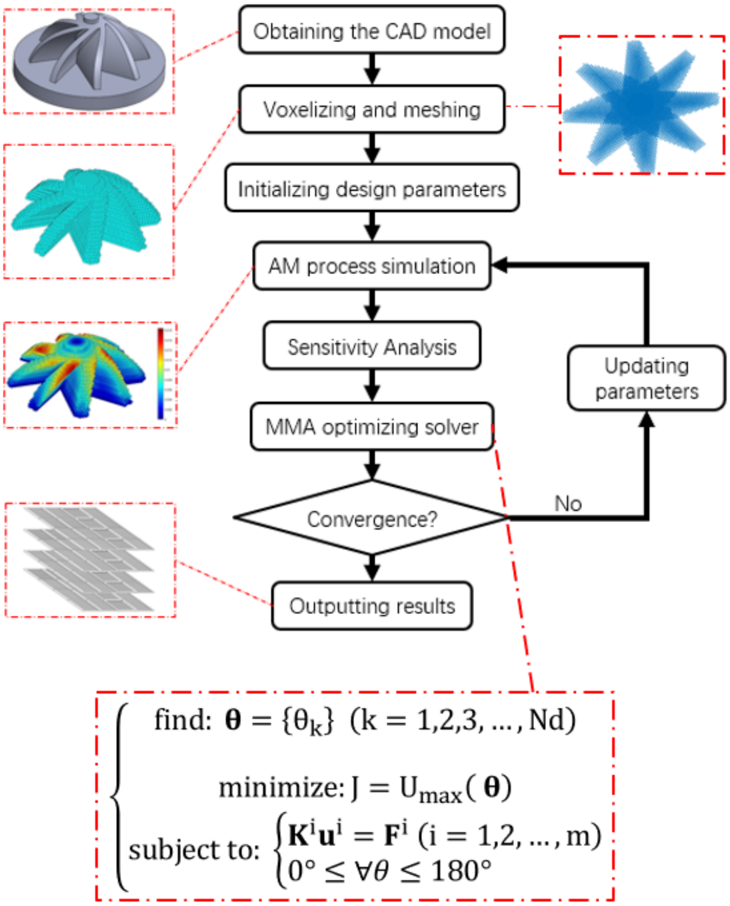

Figure 8: The process of the proposed method.

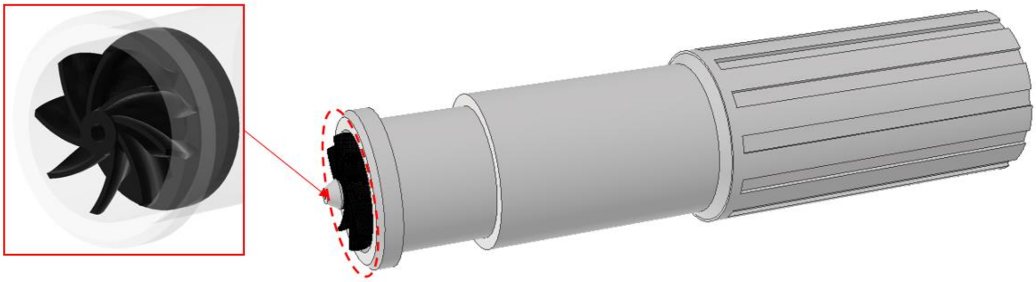

Figure 9: Road header adopted in mining machinery industry.

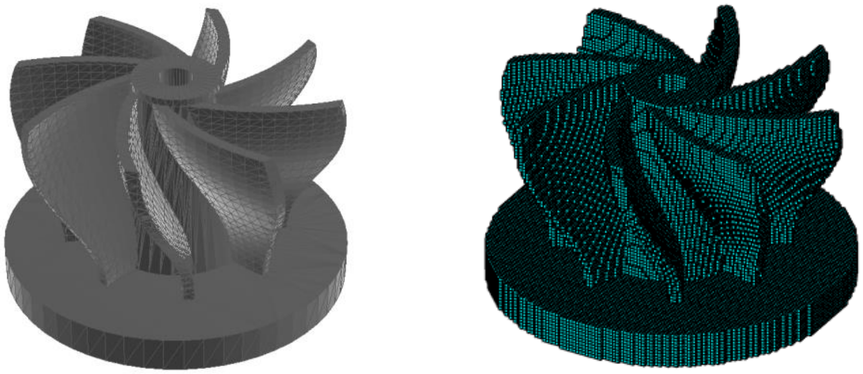

Figure 10: The STL model and voxelized model for the fan blade.

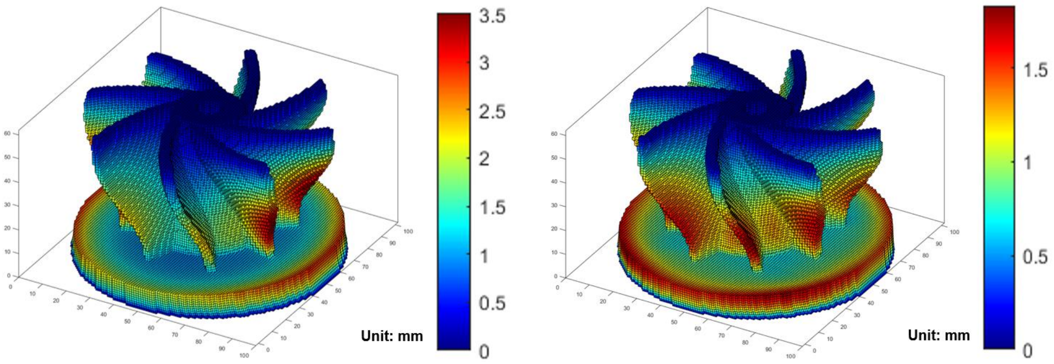

(a) (b)

Figure 11: (a) The part-scale distortion distribution for the part with default scanning path; (b) The part-scale distortion distribution for the part with optimized scanning path.

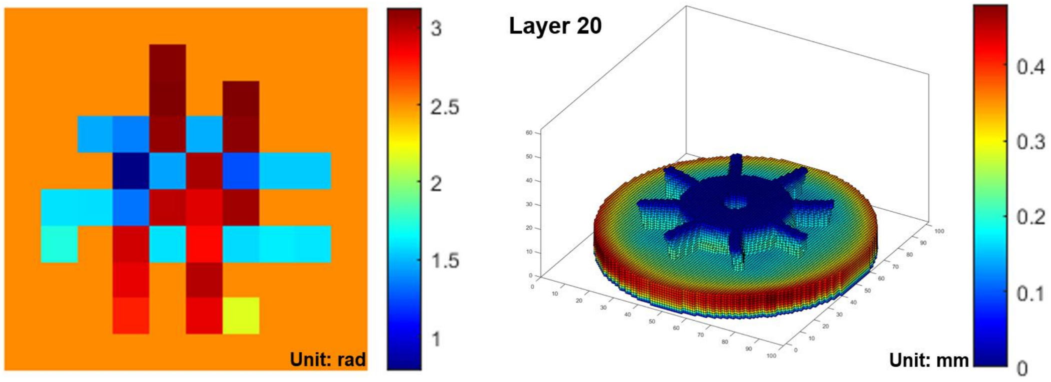

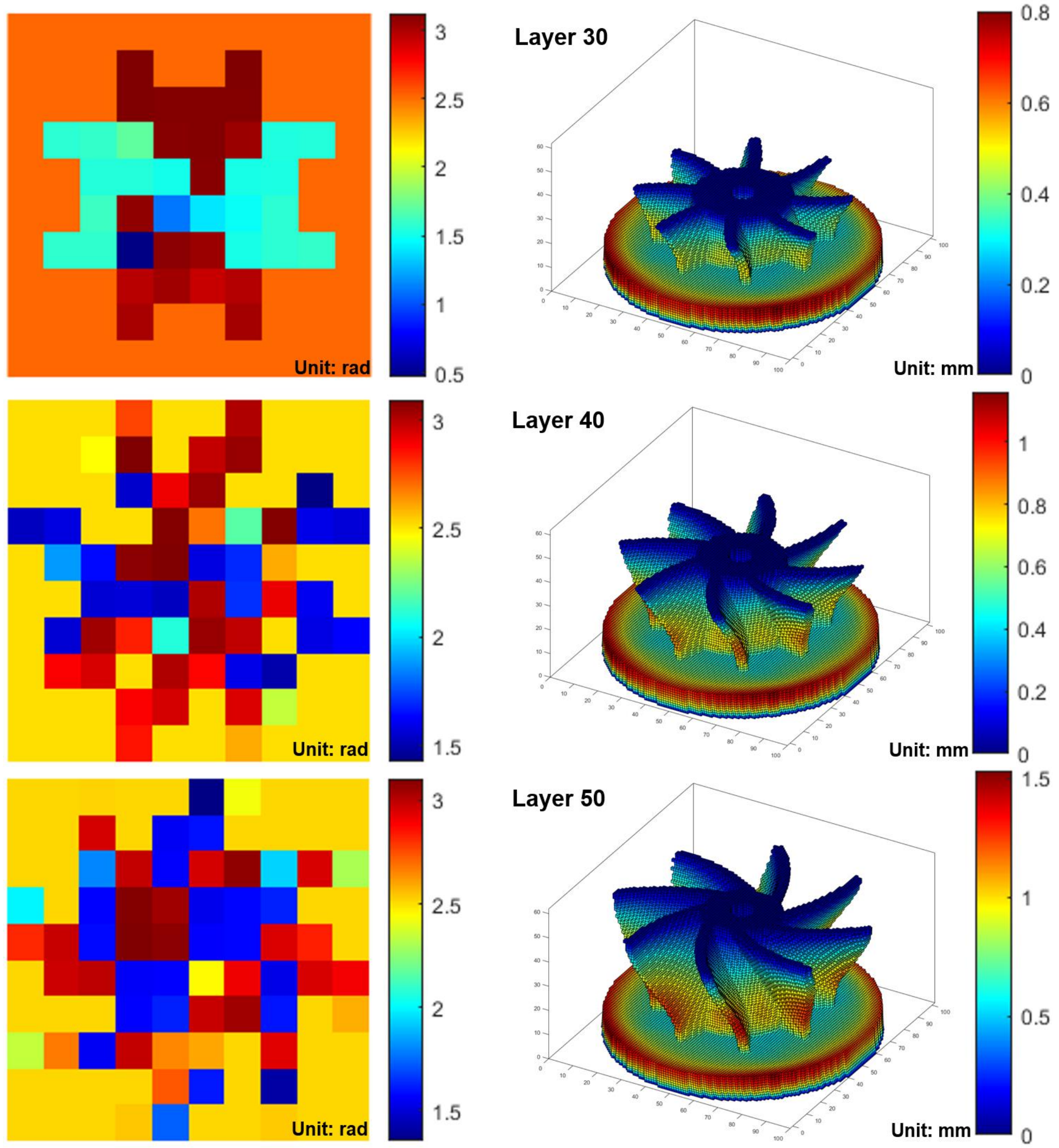

Figure 12: The distortions for the part and optimized scanning path: layer 20, layer 30, layer 40, and layer 50.

The convergence history curve for the optimization process is proposed in Figure 13. As the number of iterations increases, the objective value (blue line) is reduced and finally approached to a fixed value. Again, as we mentioned before, this optimization problem is non-constrained and the design variables are independent with each other, that is the reason why a smooth and sufficient convergence could be obtained within only 24 iterations. Additionally, the difference between the aggregated nodal maximum displacement value and real nodal maximum displacement is also plotted in Figure 13. The difference value is getting smaller and smaller with the number of iterations increasing, and it finally stabilized at 1e-8.

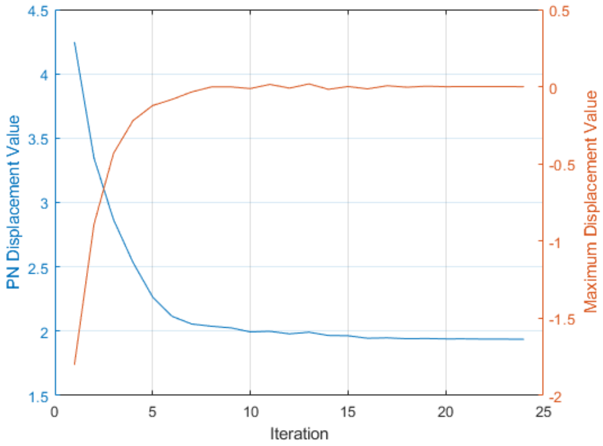

Figure 13: The convergence history plot.

7 CONCLUSION

The proposed method could successfully reduce the distortion induced by the metal AM process through optimizing the laser scanning path. A typical AM oriented part is studied to examine the performance of this method. We compare the part-scale residual distortion distribution between the parts printed by different scanning path strategy. It is found that the scanning path plays an important role for distortion minimization, and the part printed by the optimized scanning path exhibits better performances (smaller maximum distortion). Besides, a fast and stable convergence curve shown in Figure 13 also indicates the efficiency of the proposed method. Thus, this method is possible to ensure the manufacturability of AM builds. Note that although the proposed methodology obtains a good result within the numerical simulation, further demonstration of the efficiency of the proposed method is still needed. In the future, the experiment will be supplemented.

REFERENCES

[1] Allaire, G.; Jakabčin, L.: Taking into account thermal residual stresses in topology optimization of structures built by additive manufacturing, Math Models Methods Appl Sci, 28, 2018, 2313–66. https://doi.org/10.1142/S0218202518500501.

[2] Bugatti, M.; Semeraro Q. Limitations of the inherent strain method in simulating powder bed fusion processes, Additive Manufacturing, 23, 2018, 329–46. https://doi.org/10.1016/j.addma.2018.05.041.

[3] Chen, Q.; Liu, J.; Liang, X.; To, A.C.: A level-set based continuous scanning path optimization method for reducing residual stress and deformation in metal additive manufacturing, Computer Methods in Applied Mechanics and Engineering, 360, 2020, 112719. https://doi.org/10.1016/j.cma.2019.112719.

[4] Cheng, B.; Shrestha, S.; Chou, K.: Stress and deformation evaluations of scanning strategy effect in selective laser melting. Additive Manufacturing, 12, 2016, 240–51. https://doi.org/10.1016/j.addma.2016.05.007.

[5] Cheng, L.; To, A.: Part-scale build orientation optimization for minimizing residual stress and support volume for metal additive manufacturing: Theory and experimental validation, Computer-Aided Design, 113, 2019, 1–23. https://doi.org/10.1016/j.cad.2019.03.004.

[6] Cheng, L.; Liang, X.; Bai. J.; Chen, Q.; Lemon, J.; To, A.C.: On utilizing topology optimization to design support structure to prevent residual stress induced build failure in laser powder bed

metal additive manufacturing, Additive Manufacturing, 27, 2019, 290–304. https://doi.org/10.1016/j.addma.2019.03.001.
[7] Dai, L.; Shaw, L.: Distortion minimization of laser-processed components through control of laser scanning patterns, Rapid Prototyping Journal, 8, 2002, 270–6. https://doi.org/10.1108/13552540210451732.
[8] Denlinger, E.R.; Gouge, M.; Irwin, J.; Michaleris, P.: Thermomechanical model development and in situ experimental validation of the Laser Powder-Bed Fusion process, Additive Manufacturing, 16, 2017, 73–80. https://doi.org/10.1016/j.addma.2017.05.001.
[9] Foroozmehr, E.: Kovacevic R. Effect of path planning on the laser powder deposition process: thermal and structural evaluation, Int J Adv Manuf Technol, 51, 2010, 659–69. https://doi.org/10.1007/s00170-010-2659-6.
[10] Frazier, W.E.: Metal Additive Manufacturing: A Review, J of Materi Eng and Perform, 23, 2014, 1917–28. https://doi.org/10.1007/s11665-014-0958-z.
[11] Huang, J.; Chen, Q.; Jiang, H.; Zou, B.; Li, L.; Liu, J.; et al.: A survey of design methods for material extrusion polymer 3D printing, Virtual and Physical Prototyping n.d.:16.
[12] King, W.E.; Anderson, A.T.; Ferencz, R.M.; Hodge, N.E.; Kamath, C.; Khairallah, S.A.; et al.: Laser powder bed fusion additive manufacturing of metals; physics, computational, and materials challenges, Applied Physics Reviews, 2, 2015, 041304. https://doi.org/10.1063/1.4937809.
[13] Kruth, J-P.; Deckers, J.; Yasa, E.; Wauthlé, R.: Assessing and comparing influencing factors of residual stresses in selective laser melting using a novel analysis method, Proceedings of the Institution of Mechanical Engineers, Part B: Journal of Engineering Manufacture, 226, 2021, 980–91. https://doi.org/10.1177/0954405412437085.
[14] Liang, X.: An enhanced layer lumping method for accelerating simulation of metal components produced by laser powder bed fusion, Additive Manufacturing, 17, 2021.
[15] Liang, X.; Chen, Q.; Cheng, L.; Hayduke, D.; To, A.C.: Modified inherent strain method for efficient prediction of residual deformation in direct metal laser sintered components, Comput Mech, 64, 2019, 1719–33. https://doi.org/10.1007/s00466-019-01748-6.
[16] Liu, J.: Guidelines for AM part consolidation. Virtual and Physical Prototyping, 11, 2016, 133–41. https://doi.org/10.1080/17452759.2016.1175154.
[17] Liu, J.; Ma, Y.: A survey of manufacturing-oriented topology optimization methods, Advances in Engineering Software, 100, 2016, 161–75. https://doi.org/10.1016/j.advengsoft.2016.07.017.
[18] Liu, J.; Ma, Y-S.: 3D level-set topology optimization: a machining feature-based approach, Struct Multidisc Optim, 52, 2015, 563–82. https://doi.org/10.1007/s00158-015-1263-7.
[19] Liu, J.; Gaynor, A.T.; Chen, S.; Kang, Z.; Suresh, K.; Takezawa, A.; et al.: Current and future trends in topology optimization for additive manufacturing, Struct Multidisc Optim, 57, 2018, 2457–83. https://doi.org/10.1007/s00158-018-1994-3.
[20] Lu, Y.; Wu, S.; Gan, Y.; Huang, T.; Yang, C.; Junjie, L.; et al.: Study on the microstructure, mechanical property and residual stress of SLM Inconel-718 alloy manufactured by differing island scanning strategy, Optics & Laser Technology, 75, 2015, 197–206. https://doi.org/10.1016/j.optlastec.2015.07.009.
[21] Miki, T.; Yamada, T.: Topology optimization considering the distortion in additive manufacturing, ArXiv:200806153 [Cs, Math] 2021.
[22] Pellens, J.; Lombaert, G.; Michiels, M.; Craeghs, T.; Schevenels, M.: Topology optimization of support structure layout in metal-based additive manufacturing accounting for thermal deformations, Struct Multidisc Optim, 61, 2020, 2291–303. https://doi.org/10.1007/s00158-020-02512-8.
[23] Setien, I.; Chiumenti, M.; van der Veen, S.; San Sebastian, M.; Garciandía, F.; Echeverría, A.: Empirical methodology to determine inherent strains in additive manufacturing, Computers & Mathematics with Applications, 78, 2019, 2282–95. https://doi.org/10.1016/j.camwa.2018.05.015.

[24] Zhang, Z-D.; Ibhadode, O.; Ali, U.; Dibia, C. F.; Rahnama, P.; Bonakdar, A.; et al.: Topology optimization parallel-computing framework based on the inherent strain method for support structure design in laser powder-bed fusion additive manufacturing, Int J Mech Mater Des,16, 2020, 897–923. https://doi.org/10.1007/s10999-020-09494-x.
[25] Wildman, W.; Gaynor, G.: Topology Optimization for Reducing Additive Manufacturing Processing Distortions (No. ARL-TR-8242). Weapons and Materials Research Directorate, US Army Research Laboratory Aberdeen Proving Ground United States n.d.
[26] Xu, S.; Huang, J.; Liu, J.; Ma, Y.: Topology Optimization for FDM Parts Considering the Hybrid Deposition Path Pattern, Micromachines, 11, 2020, 709. https://doi.org/10.3390/mi11080709.